Journal of Materials Chemistry C

ROYAL SOCIETY OF CHEMISTRY

PAPER

View Article Online
View Journal | View Issue

Cite this: J. Mater. Chem. C, 2025, 13, 19683

Low-temperature solution-processed growth of ternary $(Bi_{1-x}Sb_x)_2S_3$ films

Sayali Shrishail Harke,[a] Omesh Kapur,[b] Ruomeng Huang *[b] and Chitra Gurnani *[a]

Received 30th June 2025,
Accepted 20th August 2025

DOI: 10.1039/d5tc02494c

rsc.li/materials-c

The development of low-temperature deposition methods for ternary metal chalcogenides is significant for advancing electronics and optoelectronic devices, where precise compositional control remains a key challenge. Here, we report a simple, low-temperature, and scalable *in situ* solvothermal technique for the deposition of ternary $(Bi_{1-x}Sb_x)_2S_3$ films using structurally compatible single-source precursors, $[Bi\{S_2P\{O(Pr)_2\}_3\}]$ and $[Sb\{S_2P\{O(Pr)_2\}_3\}]$. This one-pot chemical route facilitates precise control over composition and film quality without the need for additional processing steps. Compositional and structural characterisation confirmed the successful formation of orthorhombic $(Bi_{1-x}Sb_x)_2S_3$ phases across the full composition range (x = 0–1). The systematic shift in X-ray diffraction peak positions and lattice parameters with varying Sb content is consistent with Vegard's law, indicating the formation of a homogeneous, compositionally tunable ternary alloy. Scanning electron microscopy revealed pronounced morphology changes correlated with the Sb mole fraction, highlighting the influence of composition on microstructural evolution. UV-vis spectroscopy further demonstrated optical tunability, with bandgaps increasing from 1.82 to 2.04 eV as Sb content increased. These results underscore the effectiveness of precursor ratio adjustment for controlling final film composition and properties, showcasing the versatility of this low-temperature solvothermal approach for synthesising phase-pure, compositionally engineered mixed-metal chalcogenide thin films.

1. Introduction

Metal chalcogenides are an exciting class of highly tunable and anisotropic semiconductors that have attracted tremendous interest due to their distinct structures and extraordinary physicochemical properties.[1,2] These attributes position them as key candidates in next-generation technologies, including transistors,[3] sensors,[4] catalysis,[5] and energy storage systems.[6] Although early investigations were primarily centered on single-element and binary chalcogenide systems, the field has increasingly turned toward ternary materials. The incorporation of a third element offers enhanced flexibility to fine-tune critical physical parameters such as bandgap, charge carrier dynamics, and lattice interactions, thereby expanding the functional scope of these materials in advanced device engineering.[7,8] This compositional flexibility is particularly advantageous for advanced applications such as graded-bandgap solar absorbers,[9] broadband photodetectors,[10] and thermoelectric materials.[11] Furthermore, ternary compositions may exhibit improved defect tolerance, enhanced phase stability, and emergent functionalities not accessible in the binary phases.

Among the promising candidates for compositionally tunable materials are V–VI chalcogenides with the general formula M_2X_3 (M = As, Sb, Bi; X = S, Se, or Te), which exhibit a compelling combination of semiconducting properties, high refractive indices, and efficient charge transport.[12–16] In particular, bismuth sulfide (Bi_2S_3) and antimony sulfide (Sb_2S_3) are orthorhombic semiconductors (*Pnma* space group) with direct band gaps ranging from 1.2 to 2.5 eV, high absorption coefficients, and excellent environmental stability, making them suitable for applications in photovoltaics, photodetectors, thermoelectrics, and gas sensing devices.[17–25] More importantly, their similar oxide states and closely matched lattice parameters (differing by less than 3.5%) allow for the formation of a full range of solid solution between Bi_2S_3 and Sb_2S_3 with minimal lattice strain.[26,27] This structural compatibility has led to increasing interest in the ternary $(Bi_{1-x}Sb_x)_2S_3$ system as a compositionally tunable semiconductor platform. The ability to modulate the Bi:Sb ratio in $(Bi_{1-x}Sb_x)_2S_3$ could open new opportunities for tailoring key properties such as bandgap, carrier concentration, and thermal conductivity, parameters critical for the performance of next-generation optoelectronic[28–30] and thermoelectric devices.[31,32]

Despite extensive research on the binary end-members Bi_2S_3 and Sb_2S_3, investigations into the ternary Bi–Sb–S

[a] Ecole Centrale School of Engineering, Mahindra University (MU), Hyderabad, India. E-mail: chitra.gurnani@mahindrauniversity.edu.in
[b] School of Electronics and Computer Science, University of Southampton, Southampton, UK. E-mail: r.huang@soton.ac.uk

system—particularly $(Bi_{1-x}Sb_x)_2S_3$—remain limited and have largely focused on bulk powders rather than thin films. Kyono and co-workers synthesized a full-range $(BiSb)_2S_3$ solid solution by heating Bi_2S_3 and Sb_2S_3 together at elevated temperatures (800–1000 °C).[33] However, the high-temperature route offered limited stoichiometric precision, as multiple samples with similar compositions were produced from starting mixtures of identical Bi : Sb molar ratios. While most previous studies have relied on multiple-source precursor strategies, only two reports have investigated the ternary $(Bi_{1-x}Sb_x)_2S_3$ system using single-source precursor (SSP) chemistry: Alqahtani *et al.* synthesized powder forms *via* solventless thermolysis of metal xanthate precursors,[34] while Kun *et al.* employed thermal decomposition of piperidinedithiocarbamate complexes[35] in high-boiling solvents like oleylamine, both requiring temperatures exceeding 230 °C. These studies demonstrated the feasibility of forming ternary phases but offered limited compositional control, scalability, and phase purity due to the use of complex, multi-step processes and powder-based systems. While nature occasionally exhibits compositional variation in Bi/Sb-rich sulfide systems, such as abrupt shifts in Bi/(Bi + Sb) molar ratios during hydrothermal mineralization due to semimetal boiling phenomena,[33,36,37] synthetic control of such ternaries in thin-film form remains a significant challenge, particularly *via* solution-based routes. This underscores the need for robust, low-temperature, and scalable methods to access phase-pure $(Bi_{1-x}Sb_x)_2S_3$ films with precise compositional control.

To date, film deposition of ternary bismuth antimony sulfides has predominantly been carried out using multi-precursor systems, such as the dip-dry method,[38] chemical bath deposition,[39,40] spray pyrolysis,[41,42] and electrophoretic deposition.[43] These techniques typically require multistep processing, elevated deposition or annealing temperatures (often exceeding 200 °C), and involve precursor species with differing chemical reactivities. As a result, achieving uniform mixing, accurate stoichiometric control, and high phase purity becomes challenging. Such complexities hinder reproducibility and scale-up potential, thereby limiting the viability of these methods for commercial or large-area applications. Notably, there have been no prior reports on the deposition of $(Bi_{1-x}Sb_x)_2S_3$ films using the SSP strategy, leaving a significant gap in the development of streamlined, compositionally tunable synthesis routes for these materials. SSP strategies offer several intrinsic advantages, including cost-effectiveness, less toxicity, high material purity, and controlled film morphology. By incorporating both the metal and chalcogen within a single molecular framework, SSPs facilitate a more controlled and efficient route for material deposition. This strategy supports low-temperature and environmentally benign deposition processes, while tailored ligand architectures enable precise tuning of properties such as atomic efficiency, volatility, and overall material quality. Moreover, SSPs offer enhanced stability, precise stoichiometric control, and mitigation of pre-reactions, along with tunable thermal decomposition profiles that support optimized material growth.[44,45] In the case of ternary Bi–Sb–S systems, traditional approaches typically require more than two independent precursors, requiring careful synchronization of deposition conditions to obtain uniform solid solutions. In contrast, the use of just two well-defined and chemically compatible SSPs enables systematic and controllable access to the full compositional range of $(Bi_{1-x}Sb_x)_2S_3$. This approach facilitates reproducible synthesis of phase-pure films, even at intermediate compositions, while simplifying the overall deposition protocol. Furthermore, the ability to perform film growth under mild conditions, particularly at low temperatures, offers additional benefits, including compatibility with flexible or polymer-based substrates and reduced energy input during processing. Solution-based deposition from SSPs is inherently scalable, environmentally benign, and operationally straightforward, eliminating the need for binders, post-deposition annealing, or harsh reaction environments. Despite these advantages, the *in situ* deposition of $(Bi_{1-x}Sb_x)_2S_3$ films *via* low-temperature solvothermal routes using dithiophosphate-based SSPs remains largely unexplored. This work addresses the gap by demonstrating a facile, compositionally tunable synthesis method for ternary Bi–Sb–S chalcogenides *via* molecularly engineered SSP chemistry.

To the best of our knowledge, this is the first report of ternary $(Bi_{1-x}Sb_x)_2S_3$ film deposition *via* a low-temperature, *in situ* solvothermal route using molecularly tailored dithiophosphate-based SSPs. By systematically tuning the molar ratios of $[Bi\{S_2P(OC_3H_7)_2\}_3]$ and $[Sb\{S_2P(OC_3H_7)_2\}_3]$, we achieved controlled incorporation of Bi and Sb across the full compositional range, yielding homogeneous, phase-pure films under mild conditions. Our solution-processed approach overcomes the limitations of previous powder-based methods and offers a scalable, compositionally tunable strategy for fabricating complex chalcogenide films, with industrial compatibility suited for mass production and roll-to-roll manufacturing. The structural properties across the ternary $(Bi_{1-x}Sb_x)_2S_3$ films were evaluated by X-ray diffraction (XRD), while scanning electron microscopy (SEM) and energy-dispersive X-ray spectroscopy (EDX) confirmed the morphological consistency and compositional homogeneity of the films. Raman spectroscopy further validated the formation of well-alloyed solid solutions through composition-dependent vibrational shifts. UV-visible spectroscopy was employed to probe the optical response, revealing systematic bandgap tunability with composition. This reproducible, scalable, and environmentally benign method provides a chemically versatile route for depositing Bi–Sb–S chalcogenides with potential relevance to electronic and optoelectronic applications.

2. Experimental

2.1 Synthesis and characterisation of $[M\{S_2P(OC_3H_7)_2\}_3]$ (M = Bi (1), Sb (2)) precursors

$SbCl_3$ (99%, Sigma-Aldrich), $BiCl_3$ (99%, Sigma-Aldrich), and P_2S_5 (99%, Sigma-Aldrich), Ethanol (99.9%, Analytical reagent), triethylamine (99%, SDFine), dichloromethane (DCM) (99.5%, FINAR), and *n*-hexane (99%, SRL) were used as supplied. Toluene (99.5%, SDFine) and propan-1-ol (99%, FINAR) were freshly distilled before use. The bismuth(III) and antimony(III)

O,O′-dipropyldithiophosphate complexes, $[Bi\{S_2P(OC_3H_7)_2\}_3]$[46] (1) and $[Sb\{S_2P(OC_3H_7)_2\}_3]$[47] (2), were synthesized according to reported procedures by reacting $BiCl_3$ or $SbCl_3$ with $[Et_3NH][(OC_3H_7)_2S_2P]$ in a 3 : 1 molar ratio of ligand to metal in toluene. Comprehensive spectroscopic characterization of these precursors, including FTIR, $\{^1H\}$ NMR, and $^{31}P\{^1H\}$ NMR analyses, has also been described earlier.[46,47]

Fourier transform infrared (FT-IR) spectra were obtained using a Nicolet iS5 spectrometer (Thermo Scientific). Proton and phosphorus nuclear magnetic resonance spectra ($\{^1H\}$ and $^{31}P\{^1H\}$ NMR) were recorded at room temperature in $CDCl_3$ using a Bruker Avance Neo 500 MHz spectrometer.

2.2 Growth of $(Bi_{1-x}Sb_x)_2S_3$ films *via in situ* solvothermal deposition

Ternary bismuth–antimony sulfide $(Bi_{1-x}Sb_x)_2S_3$ films were deposited on SiO_2/Si substrates using a one-step *in situ* solvothermal technique. Fig. 1 illustrates the schematic representation of the *in situ* solvothermal method for the growth of $(Bi_{1-x}Sb_x)_2S_3$ films. The single-source precursors $[Bi\{S_2P(OC_3H_7)_2\}_3]$ (1) and $[Sb\{S_2P(OC_3H_7)_2\}_3]$ (2), previously reported by our group, were employed for the deposition of Bi_2S_3 and Sb_2S_3 films, respectively. Prior to deposition, SiO_2/Si substrates were ultrasonically cleaned in deionized water, isopropanol, and acetone to remove surface contaminants. For the synthesis of ternary compositions, the precursors (1) and (2) were mixed in various molar ratios (Bi : Sb = 1 : 1, 2 : 1, 3 : 1, and 4 : 1) and dispersed in 20 mL of ethylene glycol under continuous stirring for 1 hour. The precursor mixture formed a stable dispersion with no visible precipitation or phase separation. All dispersions were freshly prepared and used immediately to ensure uniformity and reproducibility. The resulting homogeneous solution was transferred into a 25 mL Teflon-lined stainless steel autoclave containing a horizontally placed cleaned SiO_2/Si substrate. The autoclave was sealed and heated at 180 °C for 24 hours. These conditions were chosen based on prior process optimization for the binary systems using the same precursors and deposition route,[46,47] ensuring consistent film formation and reproducibility. After naturally cooling to room temperature, the films were retrieved and vacuum-dried for 12 hours to yield uniform black films. The as-synthesized films were uniform, adherent, and obtained without the need for post-deposition annealing.

2.3 Precursor and film characterisation

Structural, compositional, morphological, vibrational, and optical characterizations were carried out using X-ray diffraction (XRD), energy-dispersive X-ray spectroscopy (EDX), scanning electron microscopy (SEM), Raman spectroscopy, and UV-visible absorption spectroscopy. XRD analysis was carried out on a Rigaku SmartLab diffractometer equipped with Cu Kα radiation (λ = 1.5406 Å), operated at 40 kV and 50 mA. Diffraction patterns were collected over a 2θ range of 10°–75°. The structural analysis was performed using reference patterns from the Inorganic Crystal Structure Database (ICDD), accessed *via* the PDF-2 2021 software package. Morphological and compositional analysis was performed using a field-emission scanning electron microscope (FESEM, ZEISS ULTRA 55) with a working distance of 5–8 mm and an acceleration voltage of 5 keV. Elemental composition was analyzed using EDX with an Oxford Instruments INCA Wave system, operated at 20 keV and analyzed *via* INCA-Point & ID software. Raman spectra were recorded on a Horiba Scientific Raman spectrometer equipped with a 633 nm laser excitation source and an optical microscope; measurements were carried out at 10% laser power to avoid sample degradation. The spectra were recorded using an

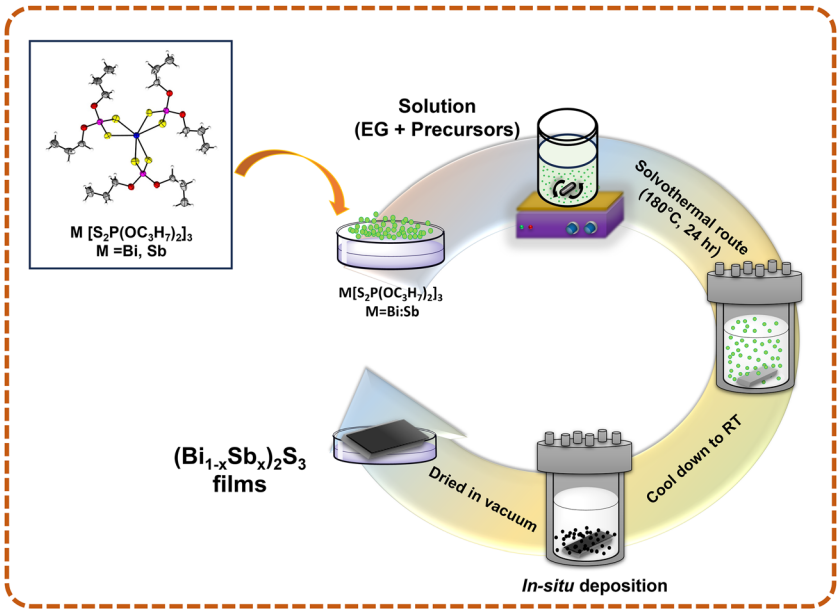

Fig. 1 Schematic representation of deposition of ternary $(Bi_{1-x}Sb_x)_2S_3$ films by *in situ* solvothermal process.

acquisition time of 10 seconds with 5 accumulations per measurement to enhance the signal-to-noise ratio. The optical bandgap of the films was evaluated using UV-vis spectroscopy (Ocean Insights) based on the diffuse reflectance method.

3. Results and discussion

3.3 Film characterization

Fig. 2 presents the EDX analysis of ternary $(Bi_{1-x}Sb_x)_2S_3$ films deposited with varying Bi to Sb precursor mole ratio. As shown in the spectra (Fig. 2(a)), distinct peaks corresponding to Bi, Sb, and S confirm the successful incorporation of all constituent elements across the compositional range. A gradual increase in Sb peak intensity and a concurrent decrease in Bi signal with decreasing Bi precursor composition indicate effective elemental substitution. Quantitative analysis (Fig. 2(b)) shows that the atomic percentage of Sb increases systematically with higher Sb precursor input, while the Bi content decreases accordingly. Sulphur content remains relatively stable (~55–65 at%), indicating near-stoichiometric incorporation independent of metal composition. The measured film compositions deviate from the initial precursor mole ratios, indicating that precise stoichiometric control is challenging when using single-source precursors $[Bi\{S_2P(OC_3H_7)_2\}_3]$ and $[Sb\{S_2P(OC_3H_7)_2\}_3]$. Such deviations are common and may arise due to differences in metal–chalcogen bond dissociation energies, which influence the decomposition kinetics and incorporation efficiency of each element.[35] In the present system, both Bi and Sb incorporations exhibit nonlinear behaviour with respect to their precursor mole fractions. The Sb content in the film follows the empirical relation (1):

$$\%\ \mathrm{Sb} = 0.4 \times \frac{\beta m}{1 + (\beta - 1)m} \qquad (1)$$

where m is the mole fraction of the Sb precursor and β is the enhancement factor. A best fit to the experimental data is achieved with $\beta = 5$, as shown in Fig. 2(b). This enhanced Sb incorporation is attributed to the differing decomposition kinetics of the Bi and Sb-based SSPs. The Bi precursor exhibits higher thermal stability, resulting in slower Bi–S bond cleavage and delayed Bi^{3+} release under solvothermal conditions. In contrast, the Sb precursor decomposes more rapidly, promoting early nucleation of Sb-rich phases. This kinetic disparity leads to preferential Sb incorporation, despite equimolar precursor ratios, and accounts for the observed deviation from linear composition.[35] These results confirm homogeneous alloy formation and demonstrate the effectiveness of this *in situ* strategy for achieving compositional tunability in ternary metal chalcogenide films.

The surface morphology of the as-deposited ternary $(Bi_{1-x}Sb_x)_2S_3$ films was systematically investigated using SEM. Fig. 3 presents SEM images of $(Bi_{1-x}Sb_x)_2S_3$ films deposited with varying Sb content (x = 0, 0.43, 0.66, 0.80, 0.85, and 1.0), illustrating the compositional influence on film morphology. Top-view SEM images (Fig. S1) reveal that the as-deposited films exhibit a compact and continuous nanostructured morphology, without visible discontinuities, indicating uniform coverage across the substrate. Notably, the morphological characteristics were strongly influenced by the Sb content (x) in the film. Bi_2S_3 film displayed hierarchical, flower-like assemblies of one-dimensional nanorods, whereas Sb_2S_3 film yielded compact sheaf-like structures composed of tightly bound rod bundles, typically conjoined near their midpoint or ends (Fig. 3(a) and (f)). A progressive and composition-dependent variation in rods was observed as the Sb film content was tuned from x = 0–1 (Fig. 3(b)–(e)). At x = 0.43, the shortest rods were observed, with a progressive increase in length seen as the Sb content increased, reaching maximum rod length at x = 0.85. Such morphological evolution is consistent with the known growth tendencies of Sb_2S_3, which favours partial fractal splitting and often produces sheaf-like architectures.[48] The introduction of Sb appears to disrupt this growth behavior, promoting more isotropic splitting and facilitating the formation of longer, radially arranged nanorods. These observations suggest that the interplay between Sb and Bi ions in the precursor solution critically influences the nucleation and growth kinetics, thereby enabling tunable morphological outcomes through precursor ratio modulation.[34,35] Wang *et al.* reported the synthesis of one-dimensional $(Bi_{1-x}Sb_x)_2S_3$ nanorods through a solution-based reaction involving bismuth and antimony chlorides,

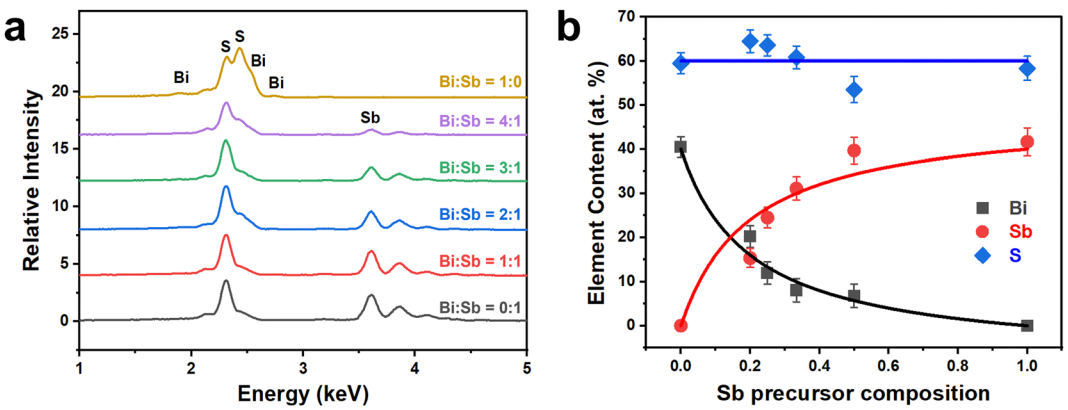

Fig. 2 (a) EDX spectra and (b) relationship between film composition and fraction of $[Sb\{S_2P(OC_3H_7)_2\}_3]$ used in the deposition of ternary $(Bi_{1-x}Sb_x)_2S_3$ films.

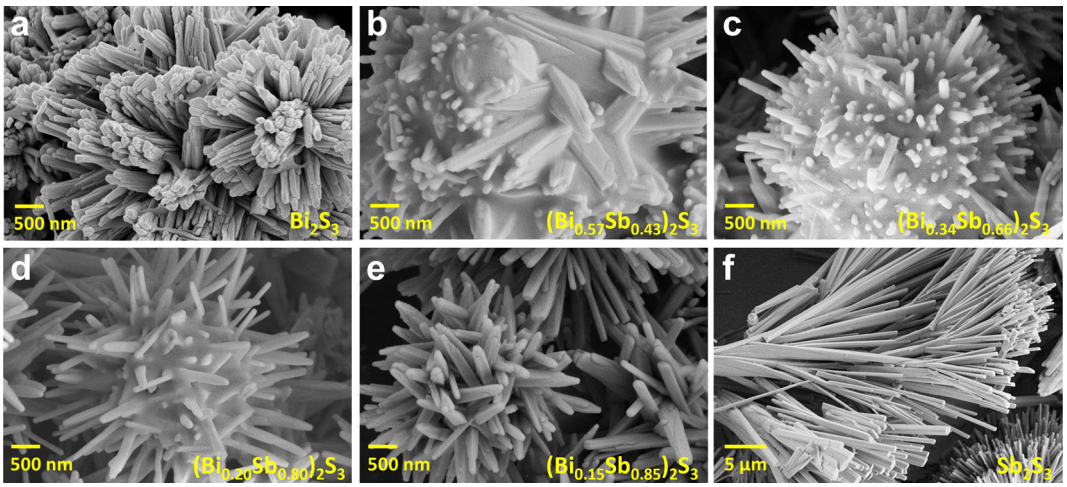

Fig. 3 SEM images showing the surface morphologies of (a) Bi_2S_3, (f) Sb_2S_3 and (b)–(e) ternary $(Bi_{1-x}Sb_x)_2S_3$ films deposited *via in situ* solvothermal process.

elemental sulfur, oleylamine, and thiols, where the rod lengths were found to be composition-dependent.[28] Similarly, Sun *et al.* fabricated flower-like Sb–Bi sulfide structures using solvothermal treatment of metal diethyldithiocarbamate complexes and suggested that the three-dimensional morphologies developed *via* epitaxial growth originating from a central Sb–Bi sulfide core.[49] Additionally, the film thickness was estimated from cross-sectional SEM analysis and found to be in the range of 40–50 μm (Fig. S2).

Furthermore, EDX elemental mapping of the ternary $(Bi_{1-x}Sb_x)_2S_3$ films with different compositions is presented in Fig. 4(b)–(e), revealing a homogeneous spatial distribution of Bi, Sb, and S across the analysed regions for all ternary films. For comparison, elemental mapping of the binary Bi_2S_3 and Sb_2S_3 films is provided in Fig. 4(a) and (f), confirming the uniform distribution of the respective constituent elements.

The crystalline quality and phase composition of the as-deposited ternary $(Bi_{1-x}Sb_x)_2S_3$ films were investigated using XRD analysis (Fig. 5(a)). All the XRD patterns for the Sb_2S_3, Bi_2S_3, and $(Bi_{1-x}Sb_x)_2S_3$ films exhibit sharp and well-defined peaks, confirming high crystallinity of the as-deposited materials, without the need for post-annealing. The diffraction patterns for all compositions correspond to an orthorhombic crystal structure, with peak positions situated between those reported for orthorhombic Bi_2S_3 (bismuthinite; ICDD card no. 17-0320; a = 11.14 Å, b = 11.29 Å, c = 3.98 Å)[46] and orthorhombic Sb_2S_3 (stibnite; ICDD card no. 42-1393; a = 11.24 Å, b = 11.31 Å, c = 3.83 Å).[47] Since both parent compounds adopt the same orthorhombic framework, the observed intermediate peak positions reflect continuous structural evolution across the compositionally tuned films. The unit cell volume contracts with increasing Sb content, consistent with the smaller ionic radius of Sb^{3+} compared to Bi^{3+}. A closer examination of the XRD patterns in Fig. 5(b), which presents a zoomed-in view over a narrower 2θ range, reveals systematic peak shifts with varying Sb content (x), indicative of compositional alloying and successful incorporation of Sb into the Bi_2S_3 lattice. The progressive shift in 2θ values for the (311), (301), and (221) planes with increasing Sb content, as shown in Fig. 5(c), further supports the formation of a homogeneous alloy, reflecting lattice expansion due to substitution of smaller Sb^{3+} ions with larger Bi^{3+} ions. The observed peak shifts across the ternary $(Bi_{1-x}Sb_x)_2S_3$ films confirm a compositionally tuned film exhibiting continuous structural integration. In addition, no secondary crystalline phases—such as elemental Sb, Bi, S, or oxide impurities (*e.g.*, Sb_2O_3, Bi_2O_3)—were observed in any of the films. The absence of any additional reflections beyond those attributed to the orthorhombic $(Bi_{1-x}Sb_x)_2S_3$ phase confirms the high phase purity and crystalline quality of the films.

Rietveld refinement of the XRD data shows that all three lattice parameters (a, b, and c) exhibit linear compositional dependence (Fig. 6(a)–(c)), consistent with Vegard's behaviour. The reliability of the refinement was supported by the calculated Rietveld parameters such as R_{wp}, R_p, goodness of fit (χ^2), and S, which are reported in Table S1. These values confirm the consistency and quality of the structural fits across the compositional series. Additionally, a representative Rietveld refinement plot has been provided in Fig. S3 to illustrate the quality of the fit. Specifically, as the Sb content increases, both the a and c lattice parameters increase, while the b parameter decreases, aligning with the expected trend when transitioning from Bi_2S_3 to Sb_2S_3. The linear variation in the lattice dimensions with Sb incorporation further supports homogeneous alloying throughout the ternary system. Interestingly, detailed analysis of the refined lattice constants reveals that both the a and c-axes follow an overall linear trend across the composition range. This anisotropic distortion may arise from the influence of stereochemically active lone electron pairs associated with the $6s^2$ (Bi) and $5s^2$ (Sb) electron configurations. These lone pairs are oriented in the a–c crystallographic plane, and while their spatial influence is distributed across this plane, the preferential deviation along the a-axis suggests a directional response, potentially driven by variations in local bonding environments and anisotropic bonding strengths between in-plane and out-of-plane directions.[50,51] As the

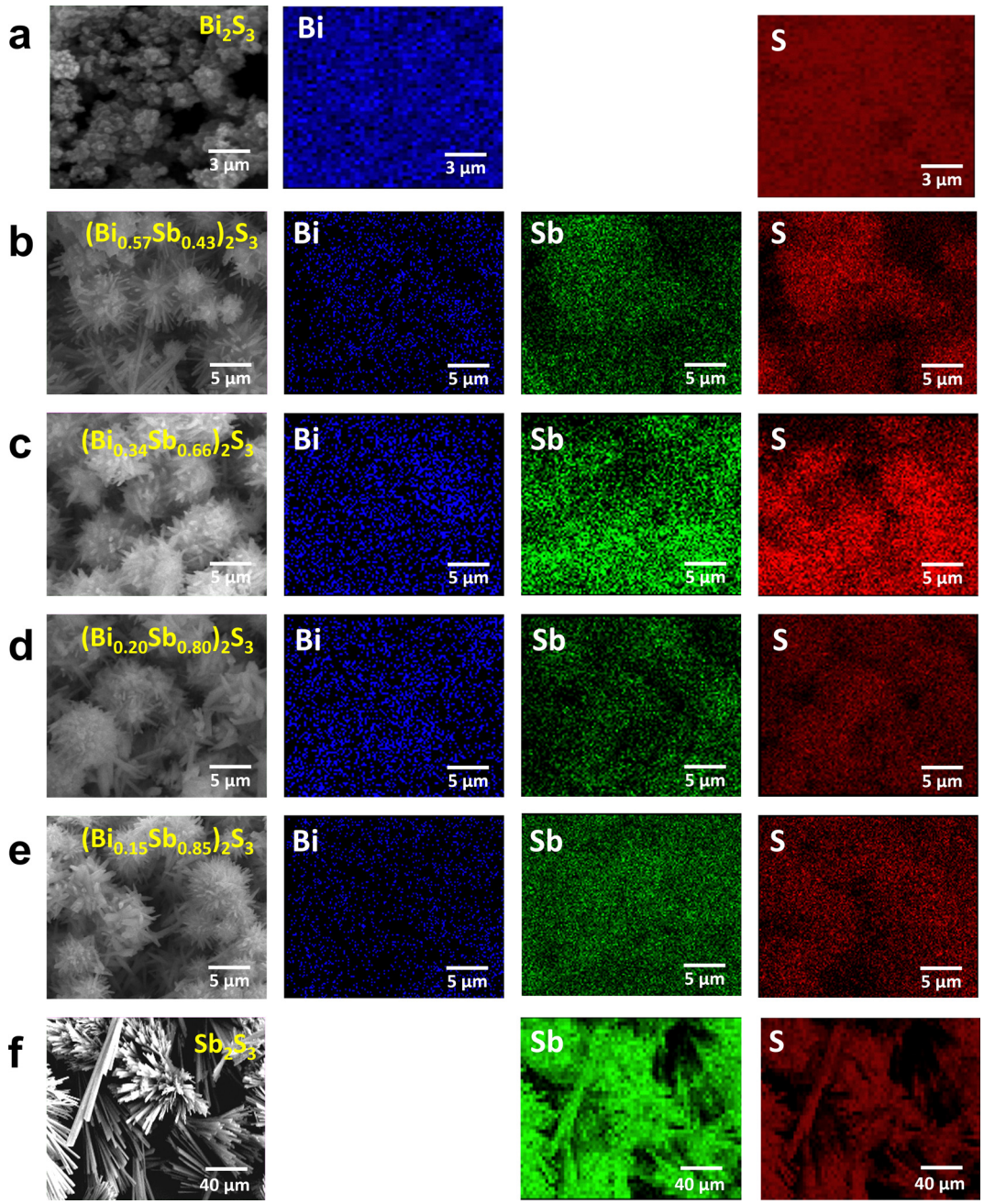

Fig. 4 EDX elemental mapping of Bi, Sb and S for (a) Bi_2S_3, (f) Sb_2S_3 and (b)–(e) ternary $(Bi_{1-x}Sb_x)_2S_3$ films deposited *via in situ* solvothermal process.

Sb content is raised, the inter-rod spacing increases due to enhanced stereochemical expression of the lone electron pair, manifesting as expansions in the *a* and *c* axes.[33] Conversely, the *b*-axis, less sensitive to lone pair influence, undergoes steady contraction with increasing Sb content, likely reflecting a reduction in the shortest M–S bond length across the solid solution from Bi_2S_3 to Sb_2S_3.[52] Overall, these structural changes culminate in a monotonic decrease in the unit cell volume with increasing Sb substitution (Fig. 6(d)), consistent with compositional tuning of the lattice through the Bi-to-Sb substitution. While EDX provides surface-sensitive elemental information, the observed compositional trends from XRD, particularly the systematic peak shifts consistent with Vegard's law, support compositional homogeneity and suggest that the bulk composition closely follows the intended stoichiometry. The crystallite size of $(Bi_{1-x}Sb_x)_2S_3$ films was estimated using the Scherrer equation. An increase in crystallite size was observed with increasing Sb content (Fig. S4), consistent with enhanced lattice distortion and refined grain morphology. Details are provided in the SI.

The vibrational properties of the as-deposited $(Bi_{1-x}Sb_x)_2S_3$ films were further investigated using Raman spectroscopy, as illustrated in Fig. 7(a). For the pure Bi_2S_3 sample, a minor peak at 178 cm^{-1} and two prominent peaks at 233 cm^{-1} and 261 cm^{-1} were observed, which correspond well with previously

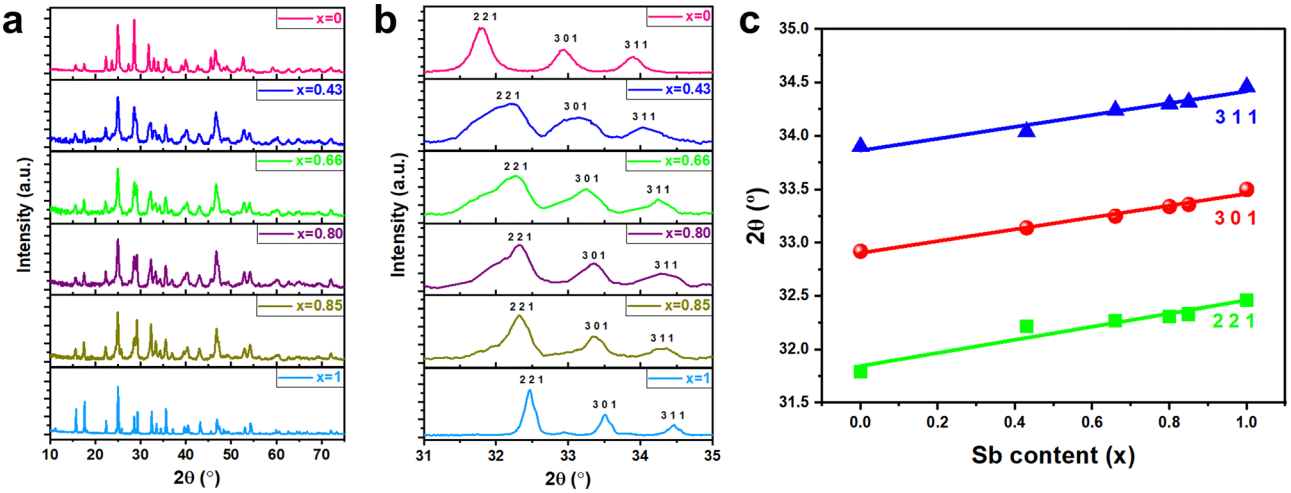

Fig. 5 (a) XRD patterns of as-deposited $(Bi_{1-x}Sb_x)_2S_3$ films for x = 0 to 1; (b) enlarged view of selected peaks showing systematic 2θ shifts with composition; (c) variation of 2θ values for the (311), (301), and (221) planes as a function of Sb content x within the $(Bi_{1-x}Sb_x)_2S_3$ films.

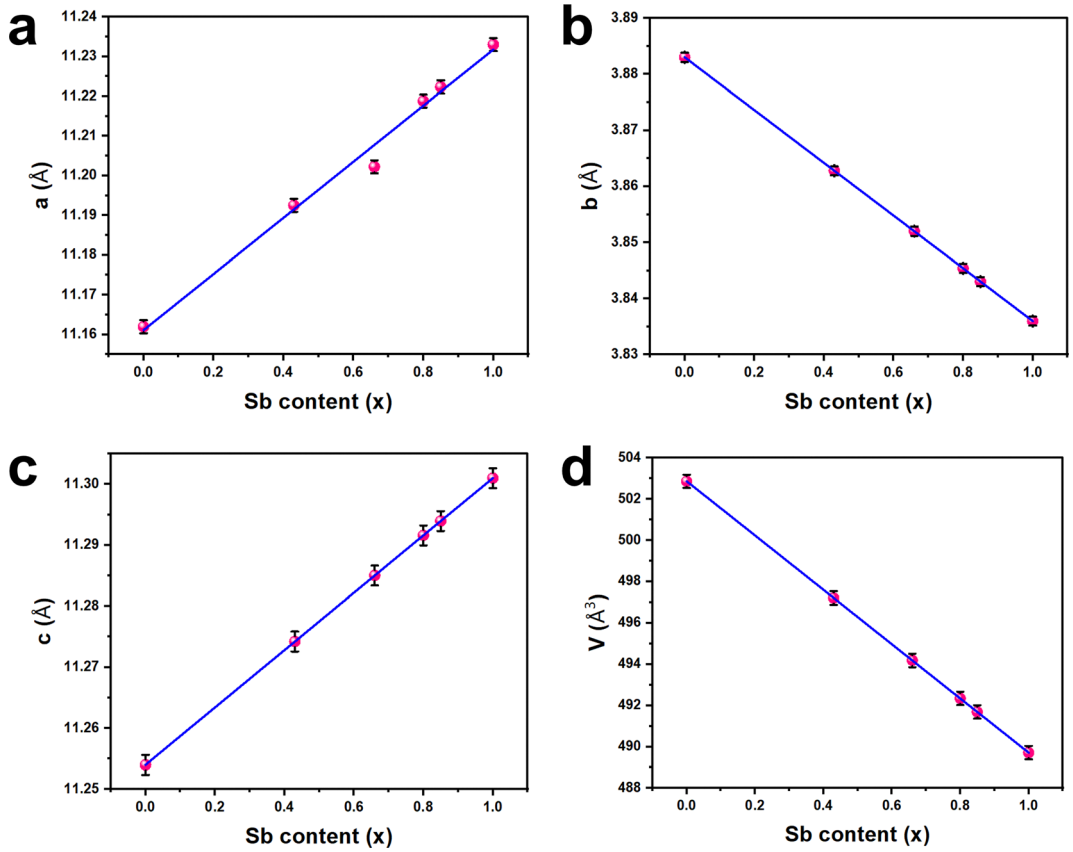

Fig. 6 Refined lattice parameters (a) a, (b) b, (c) c and (d) unit cell volume V of ternary $(Bi_{1-x}Sb_x)_2S_3$ as a function of Sb content x within the $(Bi_{1-x}Sb_x)_2S_3$ films.

reported Raman spectra for Bi_2S_3. The minor peak at 178 cm^{-1} is attributed to the A_g symmetric bending mode, while the two dominant peaks at 233 cm^{-1} and 261 cm^{-1} are assigned to the A_g and B_{1g} anti-symmetric stretching modes, respectively.[53,54] Similarly, for pure Sb_2S_3, two minor peaks at 188 cm^{-1} and 238 cm^{-1}, along with two major peaks at 279 cm^{-1} and 302 cm^{-1}, were observed, which align with previously reported data.[55–57] The peak at 188 cm^{-1} is attributed to the B_{1g} anti-symmetric S–Sb–S bending mode, while the peaks at 238 cm^{-1}, 279 cm^{-1}, and 302 cm^{-1} are associated with the Ag symmetric S–Sb–S bending

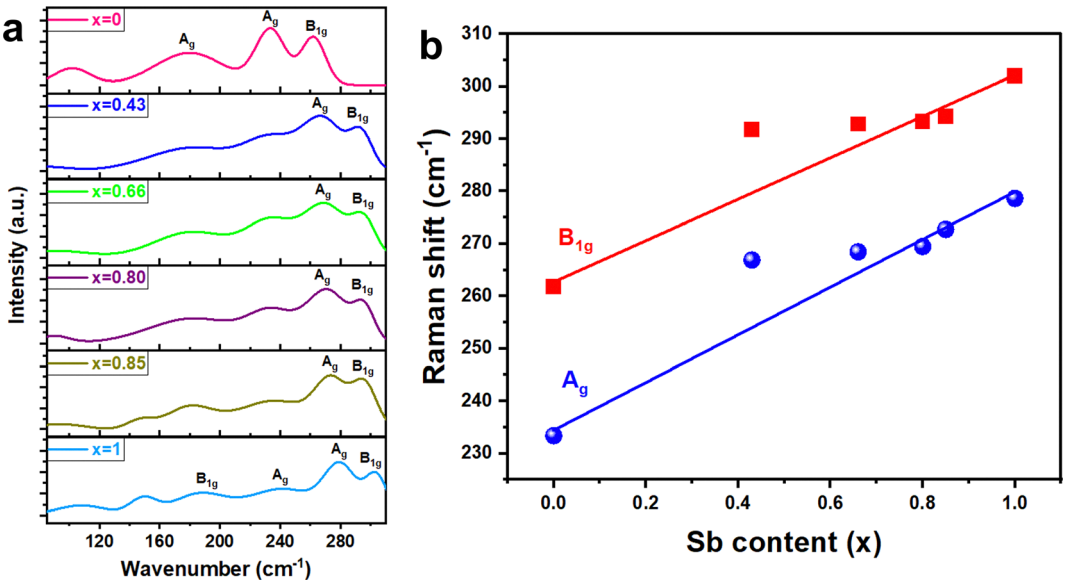

Fig. 7 (a) Raman spectra of $(Bi_{1-x}Sb_x)_2S_3$ films, (b) phonon frequencies (red: B_{1g} mode; blue: A_g mode) as a function of Sb content (x).

mode, the Ag anti–symmetric Sb–S stretching mode, and the B_{1g} anti-symmetric Sb–S stretching mode, respectively.[58,59] These vibrational modes are also present in all the ternary $(Bi_{1-x}Sb_x)_2S_3$ films, but with a progressive shift to higher wavenumbers as the Sb content increases (Fig. 7(b)). These results provide strong evidence for well-distributed compositionally tuned films.[34,35] For the film with Sb content $x = 0.85$, two broad bands centered around 273 cm^{-1} and 294 cm^{-1} were observed, which shift to lower frequencies of 267 cm^{-1} and 291 cm^{-1} when the Sb content is reduced to $x = 0.43$. The shift to higher wavenumbers when transitioning from Bi_2S_3 to Sb_2S_3 is attributed to the lower mass of Sb compared to Bi, as well as the shorter Sb–S bond lengths.[53,60]

The optical bandgap of $(Bi_{1-x}Sb_x)_2S_3$ (x = 0 to 1) films deposited on SiO_2-coated silicon substrates was investigated using Tauc plot analysis derived from UV-vis absorption spectra. The corresponding absorption spectra for the various compositions are shown in Fig. 8(a). The optical bandgap energy (E_g) was estimated by plotting $(\alpha h\nu)^2$ against photon energy ($h\nu$), where α denotes the absorption coefficient, h is Planck's constant, and ν the frequency of incident light. A linear extrapolation of the absorption edge confirmed a direct allowed transition, consistent with the known electronic properties of both Bi_2S_3 and Sb_2S_3.[25,61] As depicted in Fig. 8(b), the optical bandgap increases monotonically from 1.82 eV for Bi_2S_3 (x = 1) to 2.04 eV for Sb_2S_3 (x = 0), with intermediate

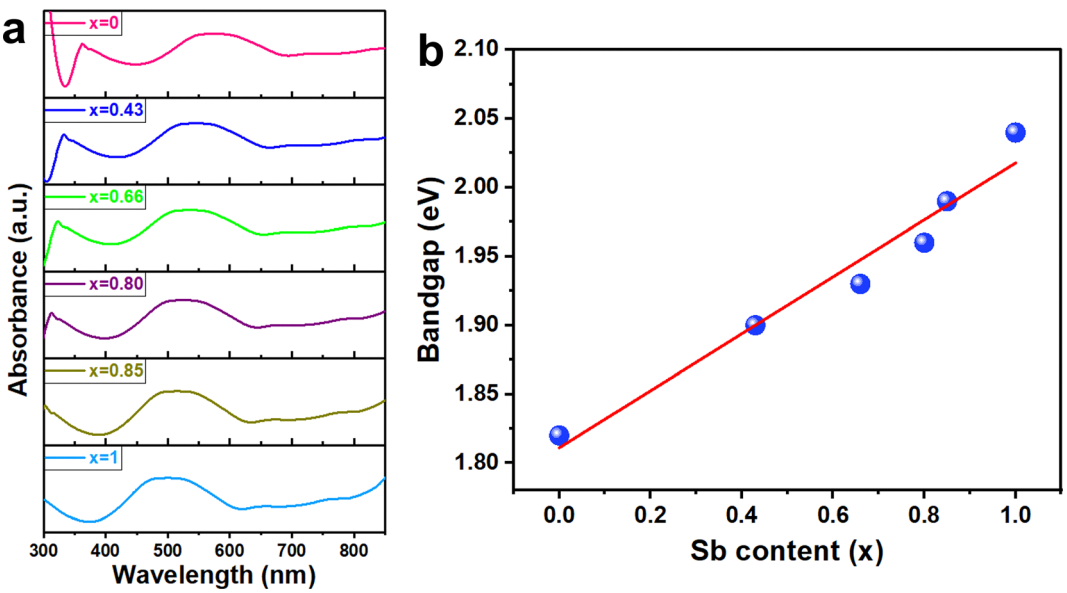

Fig. 8 (a) Absorption spectra and (b) variation of the band gap of $(Bi_{1-x}Sb_x)_2S_3$ ($0 \le x \le 1$) films as a function of Sb content (x).

compositions (x = 0.43, 0.66, 0.80, and 0.85) exhibiting bandgap values of 1.90, 1.93, 1.96, and 1.99 eV, respectively. These data points closely follow a linear compositional dependence, indicating systematic bandgap tunability across the ternary films. This continuous bandgap evolution confirms the formation of compositionally tuned films. A slight deviation from ideal linearity can be attributed to subtle stoichiometric variations within the films.[62] Overall, the results are consistent with previous reports on $(Bi_{1-x}Sb_x)_2S_3$ systems synthesized *via* solventless thermolysis of metal xanthate precursors; however, those studies were limited to powder-based materials.[34] In contrast, the present work highlights that the compositional modulation in films offers an effective strategy for tuning the optoelectronic properties of the system. Notably, the tunable bandgap range of 1.82–2.04 eV lies within the visible spectrum, making these materials promising candidates for optoelectronic devices such as photodetectors[63] and photovoltaics.[64] This moderate bandgap range enables efficient visible-light absorption while minimizing thermalization losses, offering a suitable trade-off between absorption efficiency and carrier transport in light-harvesting[9] and photoconductive applications.[65]

4. Conclusions

In this study, we have demonstrated an *in situ* solvothermal method as a low-temperature, solution-based route for the growth of ternary $(Bi_{1-x}Sb_x)_2S_3$ materials by compositionally tuning the $[Bi\{S_2P(OPr)_2\}_3]$ and $[Sb\{S_2P(OPr)_2\}_3]$ single-source precursors. Our findings show that the ternary film composition is primarily governed by the relative molar ratios of the Bi- and Sb-based precursors used during synthesis, allowing for predictable and tunable alloy formation. SEM analyses reveal that film morphology can also be modulated by precursor composition, enabling microstructural control. The resulting films exhibit orthorhombic crystal structures, with XRD peak positions systematically shifting between those of Bi_2S_3 and Sb_2S_3, consistent with Vegard's law across the full compositional range. This confirms the successful formation of homogeneous alloys and highlights the effectiveness of rapid precursor scrambling under solvothermal conditions. Furthermore, UV-vis spectroscopy confirms the optical tunability of these materials, with a systematic increase in bandgap with increasing Sb content. These results underscore the impact of nanoscale structure and composition on the optoelectronic properties of the chalcogenide material. This scalable and compositionally versatile approach demonstrates the utility of chemically compatible single-source precursors for engineering complex metal chalcogenides with controllable structural and electronic properties, offering a promising platform for future solution-processed electronic and optoelectronic applications.

Author contributions

Sayali Shrishail Harke: conceptualization, methodology, investigation, validation, formal analysis, writing – original draft. Omesh Kapur: formal analysis. Ruomeng Huang: conceptualization, Validation, Formal analysis, Writing – review & editing, Supervision. Chitra Gurnani: Conceptualization, Validation, Formal analysis, Writing – review & editing, Supervision.

Conflicts of interest

There are no conflicts to declare.

Data availability

Data for this article are available from the University of Southampton repository at **https://doi.org/10.5258/SOTON/D3621**.

The supporting information contains top-view SEM micrographs, cross-sectional images, Rietveld refinement patterns with refined lattice parameters, and details of the crystallite size analysis for the ternary $(Bi_{1-x}Sb_x)_2S_3$ films deposited *via* the *in situ* solvothermal process. See DOI: **https://doi.org/10.1039/d5tc02494c**

Acknowledgements

The authors would like to thank EPSRC (EP/Y001567/1) for funding this project. Additionally, appreciation is extended to the School of Physics, University of Hyderabad, India for granting access to the SEM facility. All data supporting this study are openly available from the University of Southampton repository a **https://doi.org/10.5258/SOTON/D3621**.

References

1 B. Zhao, D. Shen, Z. Zhang, P. Lu, M. Hossain, J. Li, B. Li and X. Duan, *Adv. Funct. Mater.*, 2021, **31**, 2105132.
2 Y. Cheng, W. Quan, J. Wang, Y. Peng, T. Zhou, H. Ding and Y. Zhang, *Small Methods*, 2025, 2402196.
3 C. Shen, Z. Yin, F. Collins and N. Pinna, *Adv. Sci.*, 2022, **9**, 2104599.
4 R. Wu, J. Hao and Y. Wang, *Small*, 2024, **20**, 2404821.
5 R. Yang, Y. Fan, Y. Zhang, L. Mei, R. Zhu, J. Qin, J. Hu, Z. Chen, Y. H. Ng, D. Voiry, S. Li, Q. Lu, Q. Wang, J. C. Yu and Z. Zeng, *Angew. Chem., Int. Ed.*, 2023, **135**, e202218016.
6 S. Palchoudhury, K. Ramasamy, J. Han, P. Chen and A. Gupta, *Nanoscale Adv.*, 2023, **5**, 2724–2742.
7 K. F. Mak and J. Shan, *Nat. Photonics*, 2016, **10**, 216–226.
8 J. Ji, X. Song, J. Liu, Z. Yan, C. Huo, S. Zhang, M. Su, L. Liao, W. Wang, Z. Ni, Y. Hao and H. Zeng, *Nat. Commun.*, 2016, **7**, 1–9.
9 O. Stroyuk, A. Raevskaya and N. Gaponik, *Chem. Soc. Rev.*, 2018, **47**, 5354–5422.
10 F. Wang, Y. Zhang, Y. Gao, P. Luo, J. Su, W. Han, K. Liu, H. Li and T. Zhai, *Small*, 2019, **15**, 1901347.
11 C. Zhou, C. Dun, K. Wang, X. Zhang, Z. Shi, G. Liu, C. A. Hewitt, G. Qiao and D. L. Carroll, *Nano Energy*, 2016, **30**, 709–716.
12 R. Suarez, P. K. Nair and P. V. Kamat, *Langmuir*, 1998, **14**, 3236–3241.
13 D. Arivuoli, F. D. Gnanam and P. Ramasamy, *J. Mater. Sci. Lett.*, 1988, **7**, 711–713.

14 S. H. Pawar, P. N. Bhosale, M. D. Uplane and S. Tamhankar, *Thin Solid Films*, 1983, **110**, 165–170.
15 O. Savadogo and K. C. Mandal, *Sol. Energy Mater.*, 1992, **26**, 117–136.
16 J. J. Carey, J. P. Allen, D. O. Scanlon and G. W. Watson, *J. Solid State Chem.*, 2014, **213**, 116–125.
17 Y. Yang, Z. Pan, X. Liu, H. Dong, X. Zhang, F. Wu and N. Huo, *Adv. Opt. Mater.*, 2025, **13**, 2402501.
18 P. Terdalkar, D. D. Kumbhar, S. D. Pawar, K. A. Nirmal, T. G. Kim, S. Mukherjee, K. V. Khot and T. D. Dongale, *Solid-State Electron.*, 2025, **225**, 109076.
19 F. Anjum, D. Bhattacharjee, A. Bhattacharya and T. Maiti, *Small*, 2025, **21**, 2412711.
20 X. Chen, T. Wang, J. Shi, W. Lv, Y. Han, M. Zeng, J. Yang, N. Hu, Y. Su, H. Wei, Z. Zhou, Z. Yang and Y. Zhang, *Nano-Micro Lett.*, 2022, **14**, 1–15.
21 S. Li, J. Xu, S. Shi, L. Kong, X. Zhang and L. Li, *Chem. Eng. J.*, 2025, **511**, 161890.
22 P. Kumar, M. Q. Khan, S. Suganthi, K. Ahmad and T. H. Oh, *ChemistrySelect*, 2025, **10**, e202404430.
23 S. Tan, H. Hu, Y. Wang, L. Ma, L. Song, J. Tang, H. Zhou, K. Zheng, G. Ren and L. Yang, *J. Mater. Sci. Technol.*, 2025, **234**, 239–245.
24 S. B. Jaffri, K. S. Ahmad, B. Makawana, R. K. Gupta, M. A. Abdel-Maksoud, A. Malik and W. H. Al-Qahtani, *J. Phys. Chem. Solids*, 2025, **196**, 112394.
25 S. Chamola, R. Zhou, O. M. Bakr and S. Ahmad, *Adv. Funct. Mater.*, 2024, **35**, 2414913.
26 G. Springer, *Mineral. Mag.*, 1969, **37**, 294–296.
27 G. Springer and J. H. G. LaFlamme, *Can. Mineral.*, 1971, **10**, 847–853.
28 J. Wang, H. Yu, T. Wang, Y. Qiao, Y. Feng and K. Chen, *ACS Appl. Mater. Interfaces*, 2018, **10**, 7334–7343.
29 J. Wang, L. Jin, T. Wang, L. Zhao, F. Guan, S. Li, D. Wang and J. Zhang, *J. Alloys Compd.*, 2020, **831**, 154886.
30 B. K. Patra, S. Khilari, A. Bera, S. K. Mehetor, N. Pradhan and N. Pradhan, *Chem. Mater.*, 2017, **29**, 1116–1126.
31 Z. Zhang, R. Zhang, N. Qi, Y. Wu and Z. Chen, *Phys. Chem. Chem. Phys.*, 2020, **22**, 15559–15566.
32 B. Xu, S. Yuan, X. Liu, S. Ma, J. Zhang, Y. Wang, J. Li, Z. Gu and L. Yi, *Comput. Mater. Sci.*, 2022, **211**, 111497.
33 A. Kyono and M. Kimata, *Am. Mineral.*, 2004, **89**, 932–940.
34 T. Alqahtani, M. D. Khan, D. J. Kelly, S. J. Haigh, D. J. Lewis and P. O'Brien, *J. Mater. Chem. C*, 2018, **6**, 12652–12659.
35 W. N. Kun, P. D. McNaughter, L. D. Nyamen, B. F. Spencer, P. O'Brien, P. T. Ndifon and N. Revaprasadu, *RSC Adv.*, 2019, **9**, 15836–15844.
36 S. Ghosal and R. O. Sack, *Mineral. Mag.*, 1999, **63**, 723–733.
37 V. W. Lueth, P. C. Goodell and N. E. Pingitore, *Econ. Geol.*, 1990, **85**, 1462–1472.
38 B. B. Nayak, H. N. Acharya, G. B. Mitra and B. K. Mathur, *Thin Solid Films*, 1983, **105**, 17–24.
39 B. Meena, M. Kumar, S. Gupta, L. Sinha, P. Subramanyam and C. Subrahmanyam, *Sustain. Energy Technol. Assess.*, 2022, **49**, 101775.
40 I. M. El Radaf and H. Y. S. Al-Zahrani, *Phys. B*, 2022, **631**, 413655.
41 P. Usha Rajalakshmi, R. Oommen, C. Sanjeeviraja and V. Ganesan, *Superlattices Microstruct.*, 2013, **57**, 158–165.
42 P. Usha Rajalakshmi, R. Oommen and C. Sanjeeviraja, *Thin Solid Films*, 2013, **531**, 76–80.
43 N. P. Dileep, M. C. Madhusudhanan, L. K. Puthenveettil, V. Yadav, S. N. Myakala, S. Kunnikuruvan and M. M. Shaijumon, *ACS Appl. Energy Mater.*, 2024, **7**, 3688–3699.
44 C. Gurnani, S. L. Hawken, A. L. Hector, R. Huang, M. Jura, W. Levason, J. Perkins, G. Reid and G. B. G. Stenning, *Dalton Trans.*, 2018, **47**, 2628–2637.
45 P. N. Bartlett, C. H. K. de Groot, V. K. Greenacre, R. Huang, Y. J. Noori, G. Reid and S. Thomas, *Nat. Rev. Chem.*, 2025, **9**, 88–101.
46 S. S. Harke, Y. Jadhav, V. B. Patil and C. Gurnani, *ACS Appl. Electron Mater.*, 2025, **7**, 1291–1304.
47 S. S. Harke, T. Zhang, R. Huang and C. Gurnani, *Mater. Adv.*, 2023, **4**, 4119–4128.
48 J. Wang, Y. Qiao, T. Wang, H. Yu, Y. Feng and J. Zhang, *CrystEngComm*, 2019, **21**, 554–562.
49 J. Sun, X. Shen, L. Guo, G. Wang, J. Park and K. Wang, *Nanoscale Res. Lett.*, 2010, **5**, 364–369.
50 M. Leszczyński, E. Litwin-Staszewska, T. Suski, J. Bąk-Misiuk and J. Domagała, *Acta Phys. Pol. A*, 1995, **88**, 837–840.
51 R. A. Groom, A. Jacobs, M. Cepeda, R. Drummey and S. E. Latturner, *Inorg. Chem.*, 2017, **56**, 12362–12368.
52 D. Poleti, K. Ljiljana, B. Z. Tonci and G. Ivan, *Neues Jahrb. Mineral., Abh.*, 2012, **189**, 177–187.
53 I. Zumeta-Dubé, J. L. Ortiz-Quiñonez, D. Díaz, C. Trallero-Giner and V. F. Ruiz-Ruiz, *J. Phys. Chem. C*, 2014, **118**, 30244–30252.
54 B. Mukherjee, C. Chotia, Tarachand, R. Venkatesh and G. S. Okram, *AIP Conf. Proc.*, 2020, **2220**, 020095.
55 S. M. Hwang, J. Kim, Y. Kim and Y. Kim, *J. Mater. Chem. A*, 2016, **4**, 17946–17951.
56 J. S. Eensalu, K. Tõnsuaadu, I. Oja Acik and M. Krunks, *Mater. Sci. Semicond. Process.*, 2022, **137**, 106209.
57 M. Delaney, I. Zeimpekis, D. Lawson, D. W. Hewak and O. L. Muskens, *Adv. Funct. Mater.*, 2020, **30**, 2002447.
58 R. G. Sotelo Marquina, T. G. Sanchez, N. R. Mathews and X. Mathew, *Mater. Res. Bull.*, 2017, **90**, 285–294.
59 R. Parize, A. Katerski, I. Gromyko, L. Rapenne, H. Roussel, E. Kärber, E. Appert, M. Krunks and V. Consonni, *J. Phys. Chem. C*, 2017, **121**, 9672–9680.
60 B. Minceva-Sukarova, M. Najdoski, I. Grozdanov and C. J. Chunnilall, *J. Mol. Struct.*, 1997, **410–411**, 267–270.
61 M. A. Saifee, U. Latief, J. Ali and M. S. Khan, *Discover Energy*, 2024, **4**, 1–15.
62 F. Viñes, G. Konstantatos and F. Illas, *Phys. Chem. Chem. Phys.*, 2017, **19**, 27940–27944.
63 C. Tan, M. Amani, C. Zhao, M. Hettick, X. Song, D. H. Lien, H. Li, M. Yeh, V. R. Shrestha, K. B. Crozier, M. C. Scott and A. Javey, *Adv. Mater.*, 2020, **32**, 2001329.
64 J. Dong, H. Liu, Z. Cao, Y. Liu, Y. Bai, M. Chen, B. Liu, L. Wu, J. Luo, Y. Zhang and S. Liu, *Small*, 2023, **19**, 2206175.
65 D. Wu, Y. Chang, Z. Lou, T. Xu, J. Xu, Z. Shi, Y. Tian and X. Li, *J. Alloys Compd.*, 2017, **708**, 623–627.

